Isolating the effect of radiation-induced segregation in irradiation-assisted stress corrosion cracking of austenitic stainless steels

J.T. Busby [a,*], G.S. Was [a], E.A. Kenik [b]

[a] *University of Michigan, 2937 Cooley Building, 2355 Bonisteel Blvd. Ann Arbor, MI 48109-2104, USA*
[b] *Oak Ridge National Laboratory, Oak Ridge, TN 37831, USA*

Abstract

Post-irradiation annealing was used to help identify the role of radiation-induced segregation (RIS) in irradiation-assisted stress corrosion cracking (IASCC) by preferentially removing dislocation loop damage from proton-irradiated austenitic stainless steels while leaving the RIS of major and minor alloying elements largely unchanged. The goal of this study is to better understand the underlying mechanisms of IASCC. Simulations of post-irradiation annealing of RIS and dislocation loop microstructure predicted that dislocation loops would be removed preferentially over RIS due to both thermodynamic and kinetic considerations. To verify the simulation predictions, a series of post-irradiation annealing experiments were performed. Both a high purity 304L (HP-304L) and a commercial purity 304 (CP-304) stainless steel alloy were irradiated with 3.2 MeV protons at 360 °C to doses of 1.0 and 2.5 dpa. Following irradiation, post-irradiation anneals were performed at temperatures ranging from 400 to 650 °C for times between 45 and 90 min. Grain boundary composition was measured using scanning transmission electron microscopy with energy-dispersive spectrometry in both as-irradiated and annealed samples. The dislocation loop population and radiation-induced hardness were also measured in as-irradiated and annealed specimens. At all annealing temperatures above 500 °C, the hardness and dislocation densities decreased with increasing annealing time or temperature much faster than RIS. Annealing at 600 °C for 90 min removed virtually all dislocation loops while leaving RIS virtually unchanged. Cracking susceptibility in the CP-304 alloy was mitigated rapidly during post-irradiation annealing, faster than RIS, dislocation loop density or hardening. That the cracking susceptibility changed while the grain boundary chromium composition remained essentially unchanged indicates that Cr depletion is not the primary determinator for IASCC susceptibility. For the same reason, the visible dislocation microstructure and radiation-induced hardening are also not sufficient to cause IASCC alone. © 2002 Elsevier Science B.V. All rights reserved.

1. Introduction

Irradiation-assisted stress corrosion cracking (IASCC) is a complex form of material degradation, which occurs in reactor core components made of austenitic iron-

and nickel-base alloys. Tens or hundreds of core components may be susceptible to this form of degradation as the problem is widespread without regard to environment or alloy composition. Both microstructural effects (dislocation loop formation and radiation hardening) and microcompositional effects (radiation-induced segregation (RIS) of impurities and major alloying elements) have been identified as possible mechanisms for IASCC. While the development of both microstructural and microcompositional effects is

---

[*] Corresponding author. Tel.: 1-734 764 5225; fax: 1-734 763 4540.
E-mail address: jbusby@engin.umich.edu (J.T. Busby).

reasonably understood, the exact role each plays in IASCC is unclear.

During irradiation, the degree of segregation of major and minor alloying elements increases steadily with dose, along with changes in dislocation microstructure, hardness and cracking susceptibility as shown in Fig. 1 (taken from Ref. [1]). With increasing dose, cracking susceptibility increases at the same rate as the degree of Cr depletion, and Ni and Si enrichment (as shown in Fig. 1(a) and (b)). Phosphorous segregation is more complex, reaching a maximum level at an intermediate dose and returning to the bulk level thereafter. The complex dose dependence of P has also been observed in other studies [2–5]. Dislocation microstructure (shown as total loop line length in Fig. 1(c)) and change in yield strength (Fig. 1(d)) both reach a saturation level between 3.0 and 5.0 dpa. Given that the irradiated changes develop at similar rates, it is difficult to determine the cause of IASCC based on dose dependence alone.

High temperature annealing has been successful in eliminating irradiation-induced microstructural and microchemical changes altogether, while lower temperature anneals have been found to partially remove these features [6–8]. Potentially, an annealing condition may be found such that either microstructural or microchemical damage is removed while the other remains unaffected. With this type of annealing process, the role of RIS and/or microstructural changes in IASCC may be isolated, leading to a better understanding of the IASCC process.

The objective of this work is to determine the role of RIS in IASCC via post-irradiation annealing of proton-irradiated high purity 304L and commercial purity 304 stainless steels. Simulations of the annealing process were first utilized to determine whether microstructural damage can be removed faster than radiation-induced segregation via post-irradiation annealing, and to identify time-temperature combinations for preferential removal of loops. Measurements of grain boundary composition, dislocation loops and hardness were performed before and after annealing. Proton-irradiated tensile specimens were also annealed and strained to failure in a simulated boiling water reactor environment. Comparison of the cracking susceptibility between as-irradiated and annealed specimens showed that RIS is not a controlling factor in IASCC.
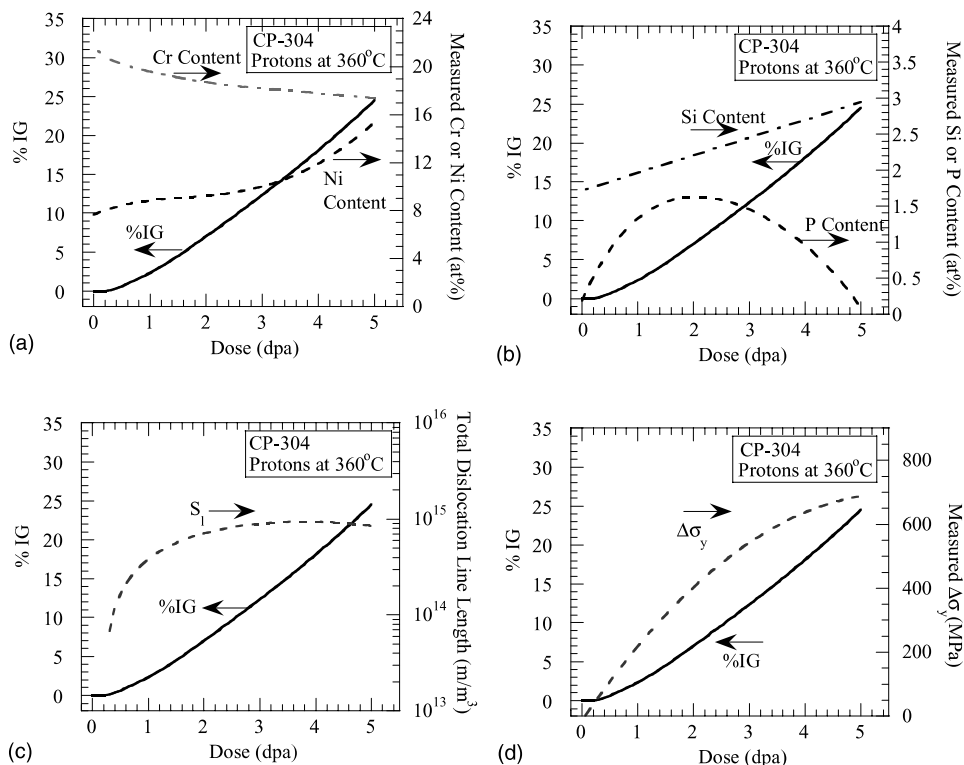

Fig. 1. Dose dependence of major alloying elements (a), minor alloying elements (b), dislocation loops (c), and hardening (d) and cracking susceptibility as a function of dose for CP-304 SS irradiated with protons at 360 °C.

2. Modeling of post-irradiation annealing

2.1. Simulated annealing of RIS

During post-irradiation annealing at low to moderate temperatures (<700 °C), the removal of composition gradients will be governed by the equilibrium vacancy concentration. The irradiation-induced composition gradients at grain boundaries will drive the motion of thermal defects during annealing. The modified inverse-Kirkendall (Perks) model developed by Allen [9] was used to simulate the behavior of composition gradients during post-irradiation annealing of 304 SS alloys. The modified inverse-Kirkendall (MIK) model is capable of handling up to three major alloying elements, and thus, was used to simulate the annealing behaviors of only Cr, Fe and Ni. For the HP-304L alloy with the nominal composition listed in Table 1, the measured segregation profile at 1.0 dpa was used as the initial condition for annealing simulations. To simulate annealing conditions, the displacement rate was simply set equal to zero. No other modifications to the model were necessary. Annealing of segregation profiles was simulated over a wide range of temperatures (350–600 °C) and times (up to 10^7 s). The annealing of grain boundary Cr depletion is shown in Fig. 2 as a function of time for anneals at 400, 500 and 600 °C. Simulations indicate that at least 10^6 s and ~1 h at 400 and 500 °C, respectively, are required to cause grain boundary depletion to be reduced to 90% of the as-irradiated condition. However, for annealing at 600 °C, 10% of the as-irradiated Cr depletion is removed in only 30 s.

2.2. Simulated annealing dislocation loops and hardness

During post-irradiation annealing, faulted, interstitial loops will absorb thermal vacancies and shrink in size. The rate of absorption, and hence rate of change in loop size, is also affected by the line tension and stacking fault energy. In order to simulate the effects of post-irradiation annealing for a population of interstitial dislocation loops, a model was developed to calculate the changes in loop radius and density as a function of time at any given temperature. For a population of defects
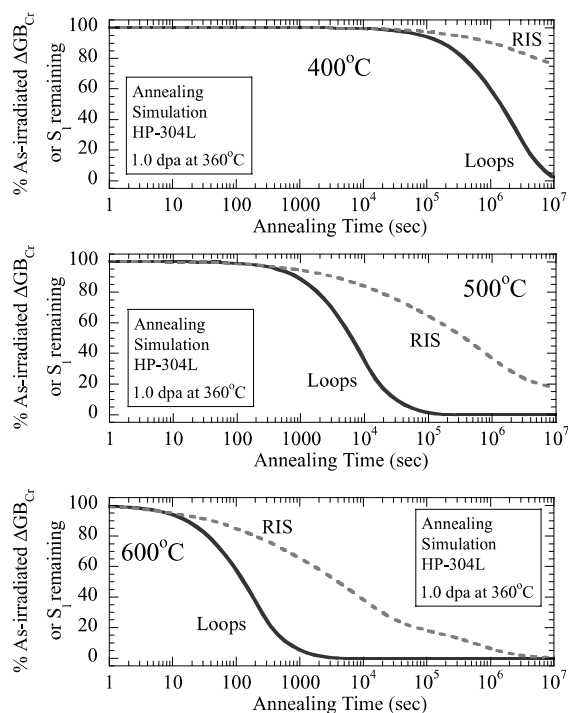

Fig. 2. Comparison of simulated annealing of fraction of as-irradiated grain boundary Cr depletion and total loop line length remaining as a function of time for anneals at 400, 500 and 600 °C. Simulation for CP-304 irradiated to 1.0 dpa at 360 °C.

widely spaced in comparison to their size, the vacancy diffusion field around each loop is assumed to be spherically symmetrical. The diffusion equation for motion of vacancies to a loop is given as

$$\frac{d}{dr}\left(r^2 D \frac{dC}{dr}\right) = 0, \tag{1}$$

where r is the radial distance from the dislocation loop, D is the vacancy diffusion coefficient, and C is the vacancy concentration. This equation can be solved by integration using the boundary conditions; $C = C_d$ at $r = r_d$ and $C = C_{eq}$ at $r = R$, where r_d is the loop radius, C_d is the vacancy concentration at the loop, R is a

Table 1
Bulk composition of HP-304L and CP-304 alloy as determined by electron microprobe analysis (wt% and at.%)

	Cr	Ni	Fe	Mn	Mo	Si	B	C	N	P	S
HP-304L											
wt%	19.7	9.5	69.7	1.12	0.02	0.01	–	0.006	<0.001	0.001	0.002
at.%	20.9	9.0	69.0	1.1	0.01	0.02	–	0.028	<0.004	0.002	0.003
CP-304											
wt%	18.3	8.5	70.6	1.38	0.37	0.65	<0.0004	0.035	0.068	0.03	0.03
at.%	19.3	7.9	69.4	1.4	0.21	1.27	<0.002	0.16	0.266	0.06	0.050

characteristic distance, and C_{eq} is the thermal equilibrium concentration of vacancies. The flux of vacancies at the loop can be written as

$$\frac{dn}{dt} = -4\pi r_d^2 \left(\frac{dc}{dr}\right)_{r=r_d} = 4\pi r_d D(C_d - C_{eq}). \qquad (2)$$

Following the methodology used by Burton [10], the rate of change of loop radius is given by

$$\frac{dr}{dt} = -2b^2 C_{eq} D\{1 - \exp(-(U/br + \Gamma/b)b^3/kT)\}, \qquad (3)$$

where $U (\approx Gb^2/2)$ is the dislocation line energy, Γ is the stacking fault energy, k is the Boltzmann constant, T is the absolute temperature, G is the shear modulus, and b is the magnitude of the Burgers vector. Note that the form of Eq. (3) indicates that larger loops are removed more slowly than smaller loops. This is reasonable, as larger loops will be more stable (i.e. less excess free energy per interstitial) and more vacancies are required to annihilate the interstitials within a larger loop.

In order to simulate the annealing behavior of a population of dislocation loops, Eq. (3) was applied to every size group within a population. For a given time step, the amount of change in loop radius and the radius at the end of the time step were calculated for each group in the population. The model then iterates over time and recalculates the rate of radius change for each group. When the radius of any group shrinks below 1 nm, the group is removed from the population, thereby reducing the dislocation loop density. While loop size distributions are informative, quantities such as total loop line length are more meaningful as they give a more complete description of the dislocation sink strength in the irradiated microstructure. Total loop line length, S_l, can be calculated as

$$S_l = 2\pi \sum_{\text{All groups,l}} r_i N_i. \qquad (4)$$

In a similar fashion, $\sqrt{Nd}$ (which is proportional to the change in yield stress according to the dispersed barrier hardening model [11]) can also be calculated.

The dislocation loop population of the HP-304L alloy irradiated with protons to 1.0 dpa at 360 °C was used as the starting condition for a series of simulated anneals over a wide range of times and temperatures. The annealing of this dislocation loop population is shown as a function of time in Fig. 2 for anneals at 400, 500 and 600 °C. As the temperature increases from 400 to 600 °C, the time to remove 10% of the as-irradiated loop population drops from 10^5 to ~10 s.

The removal of RIS and dislocation loops during post-irradiation annealing is compared directly in Fig. 2. Clearly, the simulations indicate that the dislocation microstructure is removed preferentially. In order to determine the origin of the difference in the simulated removal rates, both thermodynamic and kinetic processes are considered. Specifically, the apparent activation energy is determined for the removal of both RIS and dislocation loops. Both the density of vacancies required and potential competition for thermal vacancies between RIS and dislocation loops are also considered.

2.2.1. Thermodynamic considerations

The removal of both loops and RIS reduces the excess free energy of the system. If dislocation loop formation during irradiation increases the free energy of the system more than that due to the presence of segregation profiles, the driving force for dislocation loop removal will be greater than that for RIS. Since the annealing of both RIS and dislocation loops is dependent upon the formation and diffusion of vacancies, it may be possible to gain some insight into the energetics of the removal processes. Removal of dislocation loops and RIS during post-irradiation annealing is analogous to the removal of cold work during the recovery stage of annealing which follows a simple activation or Arrhenius type law:

$$\frac{1}{\tau} = A e^{(-Q/kT)}. \qquad (5)$$

This type of relationship was used to determine the activation energy for removing a dislocation loop population and segregation profiles. The time for removal of 90% of $1/\tau_{90}$, was determined from simulations as a function of post-irradiation annealing temperature. Simulation of microstructure annealing was accomplished using Eq. (3) and simulation of RIS was performed using the MIK model. The natural logarithm of $1/\tau_{90}$ is plotted as a function of the inverse-temperature for the annealing of both RIS and dislocation loops in Fig. 3 and the slope of the least-squares fit gives the apparent activation energy. From Fig. 3, the apparent activation energies for removal of RIS and dislocation loops are 3.1 and 2.5 eV, respectively.

The removal of both dislocation loops and RIS profiles is dependent on diffusion processes. The apparent activation energy determined from Eq. (5) and Fig. 3 for removal of RIS profiles is 3.1 eV. No combination of input diffusion parameters to the MIK model matches this value exactly, but the vacancy formation and migration energies for Ni are the closest (1.79 and 1.04 eV, respectively) [9]. The total energy required for motion via Ni atoms is 2.83 eV. While lower than the calculated value, Ni-vacancy diffusion is a sensible mechanism since both Cr depletion and Ni enrichment profiles must be removed from the grain boundary and the diffusion controlled process is limited by the rate of diffusion of the slowest participant (in this case Ni).
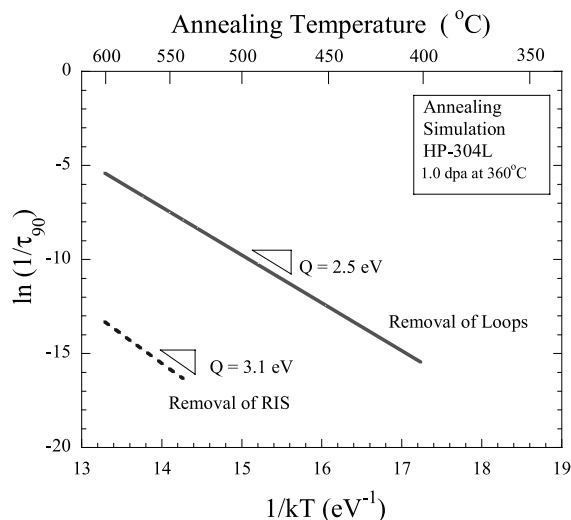
Fig. 3. Comparison of activation energies for removal of dislocation loops and RIS during simulated post-irradiation anneals of HP-304L irradiated to 1.0 dpa at 360 °C.

The annealing of dislocation loops is also dependent upon the diffusion of vacancies through the matrix. However, the stacking fault energy and line tension of the dislocation loop also influence the annealing process by reducing the energy barrier required for removal. Accounting for the stacking fault energy and line tension results in an apparent activation energy for loops which is 0.6–0.15 eV lower than that for RIS for loops ranging in size from 1 to 20 nm, respectively. The apparent activation energy for loops determined from Fig. 3 is 2.5 or 0.6 eV lower than that for removal of RIS.

2.2.2. Kinetic considerations

Although, thermodynamics are important in the annealing processes, kinetic factors may also play a role. The pre-exponential term in Eq. (5) is also of interest and was also determined to be 2.2×10^{12} s^{-1} for loops and 1.1×10^{12} s^{-1} for RIS. The difference in pre-exponential terms also gives insight into the importance of the density of defects required for annealing to be discussed in the next section. Consider the case where annealing is performed at extremely high temperatures (where $1/kT$ approaches 0). In this regime, an infinite, inexhaustible supply of vacancies is available for annealing of both RIS and loops. Yet, a difference in removal rates still exists, implying kinetics are an important consideration at low temperatures.

The most straightforward comparison between loop and RIS annealing kinetics is the number of vacancies required to remove a population of dislocation loops versus that for removal of the segregation profiles. Since the nature of the two irradiation-induced features is

different, comparisons of the number of vacancies to remove them must be made on a common scale, such as the number of defects per unit volume.

A 10.5 nm interstitial dislocation loop lying on the (1 1 1) plane is a conglomeration of $\sim$3200 interstitials. Therefore, to remove this loop entirely, a net of 3200 vacancies must be absorbed at each loop. Given a dislocation density of 4.9×10^{15} loops/cm^3, a total of 1.6×10^{19} vacancies/cm^3 are required to completely remove the dislocation loop population.

The number of vacancies required to remove the segregation profiles per cm^3 can also be calculated. The MIK code was used to track the number of vacancies passing a marker plane set at 10 nm (maximum width of RIS profile after 1.0 dpa at 360 °C). The number of vacancies was then integrated over time until the segregation profile was completely removed. For the profiles typical of 1.0 dpa irradiation, a minimum of 3.8×10^7 vacancies per 100 nm^2 of grain surface area are required to remove the segregation profiles. For 11.5 μm grains, there are approximately 5200 cm^2 of grain boundary area per cm^3. Thus, a total of 2.0×10^{23} vacancies/cm^3 are required to completely remove the segregation profiles. Comparison of the number of vacancies required for removal indicates that a factor of 2×10^4 more vacancies per cm^3 are required to remove the segregation profiles than the dislocation densities. Clearly, since fewer vacancies are required to remove dislocation loops than RIS profiles, equal defect fluxes to each sink will result in more rapid removal of dislocation loops.

Since grain boundaries and dislocation loops are both defect sinks, they may also compete for the same thermal vacancies during annealing. Specifically, if a vacancy traveling to a grain boundary passes other sinks, the probability that it reaches the grain boundary is greatly reduced. Grain boundaries act as a planar sink for defects created throughout the grain, while the dislocation loop population is a series of sinks spread throughout the grain. Note, however, that only those vacancies relatively close to the grain boundary will be influenced by the solute composition gradient and move towards the boundary to participate in annealing. The width of the vacancy concentration profile during post-irradiation annealing was investigated using the MIK code. During annealing at 500 °C, the vacancy concentration returns to the equilibrium concentration $\sim$200 nm away from the grain boundary. Therefore, within $\sim$200 nm of the grain boundary, the boundary and loops in this region compete for vacancies, while in regions more than 200 nm away, loops are the only sink for vacancies.

For the CP-304 SS at 1.0 dpa, the mean loop size is 4.9 nm and the density was 17.0×10^{21} m^{-3}. For a homogeneously distributed population, the distance between loops is, on average $\sim$110 nm. In this situation, a diffusing vacancy may encounter more than one dislo-
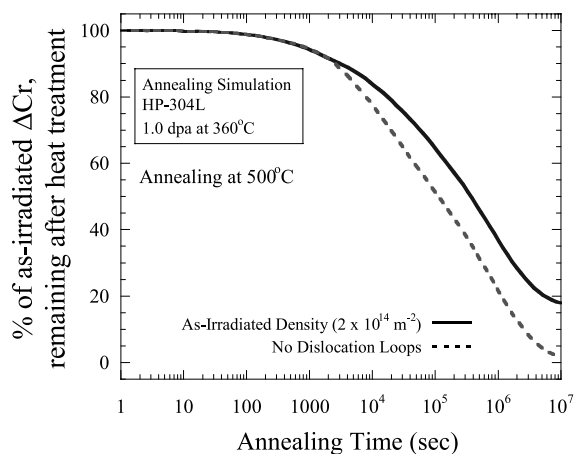
Fig. 4. Simulation of annealing of Cr segregation as a function of time during post-irradiation annealing at 500 °C, with as-irradiated dislocation density and no dislocation density.

cation loop over its diffusion path towards the grain boundary, increasing the likelihood that it will be absorbed at a loop rather than a grain boundary. Another MIK simulation was performed to evaluate the influence of the dislocation loop density on annealing of RIS profiles. Simulations of annealing at 500 °C were performed with both the as-irradiated dislocation density and with no loops. The results for the two simulations are compared in Fig. 4. Clearly, reducing the dislocation density increases the rate of annealing of RIS, which confirms that loss of vacancies to competing sinks such as dislocation loops reduces the annealing rate of RIS.

In summary, the preferential removal of dislocation loops can be explained by considering both thermodynamic and kinetic factors. Calculation of the apparent activation energy, the density of defects required for annealing, and potential competition between loops and RIS for thermal vacancies all support the preferential removal of dislocation loops during post-irradiation annealing.

3. Experimental

Table 1 lists the compositions (in wt% and at.%) for both the HP-304L and CP-304 alloys. Microstructural, microchemical, hardness and IASCC data already existed or were measured simultaneously on neutron-irradiated samples of the same CP-304 steel, allowing for a direct comparison between proton- and neutron-irradiated samples from the same heat [12]. This comparison and the dose dependence of microstructural, microchemical, hardness and IASCC for this alloy have been published elsewhere [1].

Irradiations were conducted with 3.2 MeV protons at a dose rate of approximately 7.0×10^{-6} dpa/s, resulting in a nearly uniform damage rate throughout the first 35 μm of the proton range (40 μm). The sample temperature during irradiation was maintained at 360 ± 10 °C. The HP-304L was irradiated to 1.0 dpa and the CP-304 SS alloy was irradiated to 1.0 and 2.5 dpa. Further details of the sample preparation and irradiation are given in Refs. [13,14].

Following irradiation, samples were annealed in a small tube furnace at temperatures ranging from 400 to 650 °C for times of 45 or 90 min, followed by a water quench. Samples were wrapped in stainless steel foil and immersed in flowing argon during annealing in order to reduce the oxidation of the specimen.

3.1. Radiation-induced segregation

Microchemical analysis was performed before and after annealing using a scanning transmission electron microscope with energy-dispersive X-ray analysis (STEM/EDS). The STEM/EDS analysis was performed in a Philips CM200/FEG at Oak Ridge National Laboratory, which produces a probe approximately 1.2 nm in diameter (full-width, half-maximum) while operating at 200 kV. STEM/EDS measurements were performed on 'edge-on' grain boundaries so as to minimize broadening of the boundary profile. Details of the grain boundary measurement technique are given in Ref. [15].

3.2. Radiation-induced microstructure and hardening

The dislocation microstructures of post-irradiation annealed HP-304L and CP-304 samples were analyzed using a JEOL 2010F/FEG instrument at the North Campus Electron Microscopy Analysis Laboratory at the University of Michigan and the CM200/FEG at ORNL. Bright field imaging was used to analyze the dislocation microstructure for all annealing conditions. The rel-rod dark field imaging is a more useful analysis technique as only faulted dislocation loops are visible. However, use of the dark field imaging becomes limited for low dislocation densities as it becomes increasingly difficult to detect the satellite spots created by faulted dislocation loops, as was the case for loop populations following anneals at higher temperatures. While it is easier to identify loops and measure loop sizes in a rel-rod dark field microphotograph than in a bright field microphotograph, the dislocation population relative to the as-irradiated condition is more important than the absolute value. As a result, only bright field results are presented.

For bright field imaging (BF), a two-beam condition at $g = [2\,0\,0]$ (close to the $\langle 1\,1\,0 \rangle$ zone axis) was used. This condition revealed all the faulted dislocation loops $(b = a_0/3\langle 1\,1\,1 \rangle)$ and 2/3 of perfect loops

($b = a_0/2\langle 1\,0\,0 \rangle$). Dislocation loops were most readily imaged in relatively thin regions of the TEM foil (50–100 nm thick as determined by the contamination spot method). Further, only relatively flat areas of the foil with uniform thickness were used for dislocation loop analysis. Thickness and bend contours created by wedge-shaped or warped specimens, respectively, resulted in changing diffraction conditions within the same specimen area and made dislocation loop imaging more difficult. Most dislocation loop images were taken at magnifications of 100–200 k.

Hardening for the proton-irradiated alloys was measured using a Vickers hardness indenter (MICRO-MET II) with a load of 25 g. This load was used to confine the plastic zone ahead of the indenter tip to a depth within the proton range (∼40 μm) to ensure that unirradiated material is not being sampled (as recommended by ASTM standards [16]). The change in yield stress, which is used throughout the rest of the paper, was determined from the measured change in hardness using the relation $\Delta\sigma_y = 3.6\Delta H_v$ [17].

3.3. Constant extension-rate testing

The constant extension rate tensile (CERT) tests were conducted in a multiple-specimen CERT test system, supplied by Korros Data. The Korros Data system is capable of straining four samples in parallel, thus providing identical conditions within a given test. Samples were strained to failure at a rate of 3×10^{-7} s^{-1}. Details regarding the Korros Data system are published elsewhere [1].

CERT tests were performed in normal water chemistry (NWC) characterized by a water temperature of 288 °C, water conductivity of 0.2 μS/cm and oxygen content of 2 ppm. The conductivity and oxygen composition were selected to arrive at a value of the corrosion potential of about +150 mV$_{SHE,}$ representative of BWR cores [18]. The dissolved oxygen concentration was controlled at 2 ppm by bubbling a 5% O_2/Ar mixture through the water reservoir. Conductivity was controlled via automatic additions of dilute H_2SO_4 so that the outlet conductivity was maintained at 0.2 μS/cm. The electrochemical potential was verified for the NWC environment. A Cu/CuO reference electrode with a yttria-stabilized zirconia membrane was used in conjunction with an EG&G Model 173 Potentiostat. A spare CP-304 tensile sample was used as the working electrode. For the NWC described, the measured potential was +140 mV$_{SHE}$.

Fractography was performed following each CERT test using a Philips XL30/FEG SEM. While qualitative fractography is informative in determining the type of failure and general trends, it does not provide any quantititative information about the cracking. Intergranular (IG) fracture is typically characterized by

measurements of the area of IG facets on the fracture surface and expressed as an area based percentage. However, since proton irradiation only affects the first 40 μm of the irradiated face, the majority of the fracture surface is unirradiated material. Therefore, the IG cracking fraction (or percentage) for these samples refers to the irradiated area (40 μm) only.

4. Results

4.1. Post-irradiation annealing of RIS

During post-irradiation annealing, the degree of Cr depletion did not change significantly from the irradiated condition until the most extreme annealing conditions for either the HP-304L at 1.0 dpa or the CP-304 at 1.0 and 2.5 dpa. Similarly, the amount of Ni and Fe segregation did not change appreciably. However, for the CP-304 alloy, the enrichment of minor elements such as Si and P was removed rapidly with annealing.

4.1.1. HP-304L
The results of composition measurements on samples of the HP-304L irradiated to 1.0 dpa in the as-irradiated condition and the post-irradiation annealed condition are listed in Table 2 (in at.%). The number of measurements for each condition is given in the left-most column. Typical Cr segregation profiles for each annealing condition are shown in Fig. 5(a). All plots in Fig. 5(a) also contain the as-irradiated profile (shown as open symbols) for direct comparison. Grain boundary Cr depletion remained virtually unchanged with annealing treatments below treatments of 600 °C/45 min. Annealing at 600 °C/90 min removed, on average, only 17% of the as-irradiated depletion (17.4 at.% versus 16.4 at.% in the as-irradiated case) and resulted in little change to the shape of the segregation profile while annealing at 650 °C/45 min removed 66% of the as-irradiated Cr depletion.

Similarly, the amount of grain boundary Ni enrichment also remained virtually unchanged with annealing treatments up to 650 °C/45 min, which removed virtually all as-irradiated Ni enrichment. The measured grain boundary Fe enrichment remained at or above the amount measured in the as-irradiated condition (2.5 at.% enrichment) with annealing treatments up to 600 °C/45 min. Further annealing removes additional Fe enrichment, with the grain boundary Fe content dropping to 70.4 at.% (1.4 at.% enrichment after annealing at 650 °C/45 min).

4.1.2. CP-304
The composition measurements for the CP-304 samples irradiated to 1.0 and 2.5 dpa in both the as-irradiated and post-irradiation annealed conditions are

Table 2
Summary of grain boundary composition measurements on post-irradiation annealed HP-304L (irradiated to 1.0 at 360 °C)

Irradiation condition	Fe	Cr	Ni	Mn
HP-304L matrix/bulk composition	69.0	20.9	9.0	1.1
As-irradiated 1.0 dpa				
GB average (25 measurements)	71.5	16.4	11.4	0.72
Standard deviation of mean (at.%)	0.2	0.3	0.2	0.03
500 °C/45 min				
GB average (28 measurements)	72.1	16.1	11.1	0.75
Standard deviation of mean (at.%)	0.2	0.2	0.2	0.02
500 °C/300 min				
GB average (8 measurements)	72.5	16.1	10.8	0.71
Standard deviation of mean (at.%)	0.5	0.3	0.3	0.04
550 °C/45 min				
GB average (9 measurements)	71.7	16.6	10.9	0.79
Standard deviation of mean (at.%)	0.5	0.4	0.3	0.06
600 °C/45 min				
GB average (18 measurements)	72.1	15.4	11.8	0.75
Standard deviation of mean (at.%)	0.2	0.3	0.4	0.04
600 °C/90 min				
GB average (26 measurements)	71.0	17.2	10.8	0.96
Standard deviation of mean (at.%)	0.2	0.1	0.2	0.05
650 °C/45 min				
GB average (13 measurements)	70.4	19.4	9.2	0.96
Standard deviation of mean (at.%)	0.5	0.6	0.4	0.05

All results are listed in at.%

summarized in Table 3 (in at.%) and shown in Fig. 5(b) and (c) for the 1.0 and 2.5 dpa samples, respectively. At 1.0 dpa, both the degree of Cr depletion and shape of the Cr segregation profiles remained virtually unchanged for all annealing treatments. In the as-irradiated condition, the Cr segregation profile has a 'w-shape', that is, the minimum in composition is on either side of the grain boundary with a local maximum in concentration at the grain boundary. Following anneals at 400, 450 and 500 °C for 45 min, the minimum in measured Cr content near the grain boundary is unchanged from the as-irradiated level. The Cr content at the grain boundary Cr content increased slightly with annealing, although, the as-irradiated and all annealed GB Cr contents at the peak of the 'w-shape' were measured at levels above the bulk content. Of more significance is that the complex, 'w-shape' segregation profiles remained unchanged. Even annealing at 600 °C/90 min, did not alter the as-irradiated GB Cr content or the segregation profiles. Similarly, the amount of grain boundary Ni enrichment remained unchanged with all annealing treatments while the degree of grain boundary Fe depletion was slightly altered with all annealing treatments as listed in Table 3.

Contrary to Cr, Fe and Ni, grain boundary Si changed significantly during post-irradiation annealing as shown in Table 3. The grain boundary Si enrichment was reduced steadily with annealing, with only 0.2 at.% enrichment remaining after annealing at 600 °C/90 min. Grain boundary P also changed drastically during post-irradiation annealing. Following annealing at 400 °C/45 min, the grain boundary P content has dropped to nearly the bulk level (from 1.47 at.% in the as-irradiated condition) where it remains for all other annealing treatments.

For the samples irradiated to 2.5 dpa, the grain boundary Cr profiles remained virtually unchanged with all annealing treatments. Contrary to the 1.0 dpa case the higher dose produces a more traditional 'v-shape' profile and a higher degree of Cr depletion. Annealing at 600 °C for 90 min did not alter the as-irradiated GB Cr content or the segregation profiles for the CP-304 irradiated to 2.5 dpa as illustrated in Fig. 5(c). The grain boundary Ni and Fe content remained relatively unchanged from the as-irradiation condition, similar to the 1.0 dpa samples.

Similar to the 1.0 dpa case, grain boundary Si changed significantly during post-irradiation annealing with the grain boundary Si content dropping significantly with increasing annealing time or temperature with only 0.3 at.% enrichment remaining after annealing
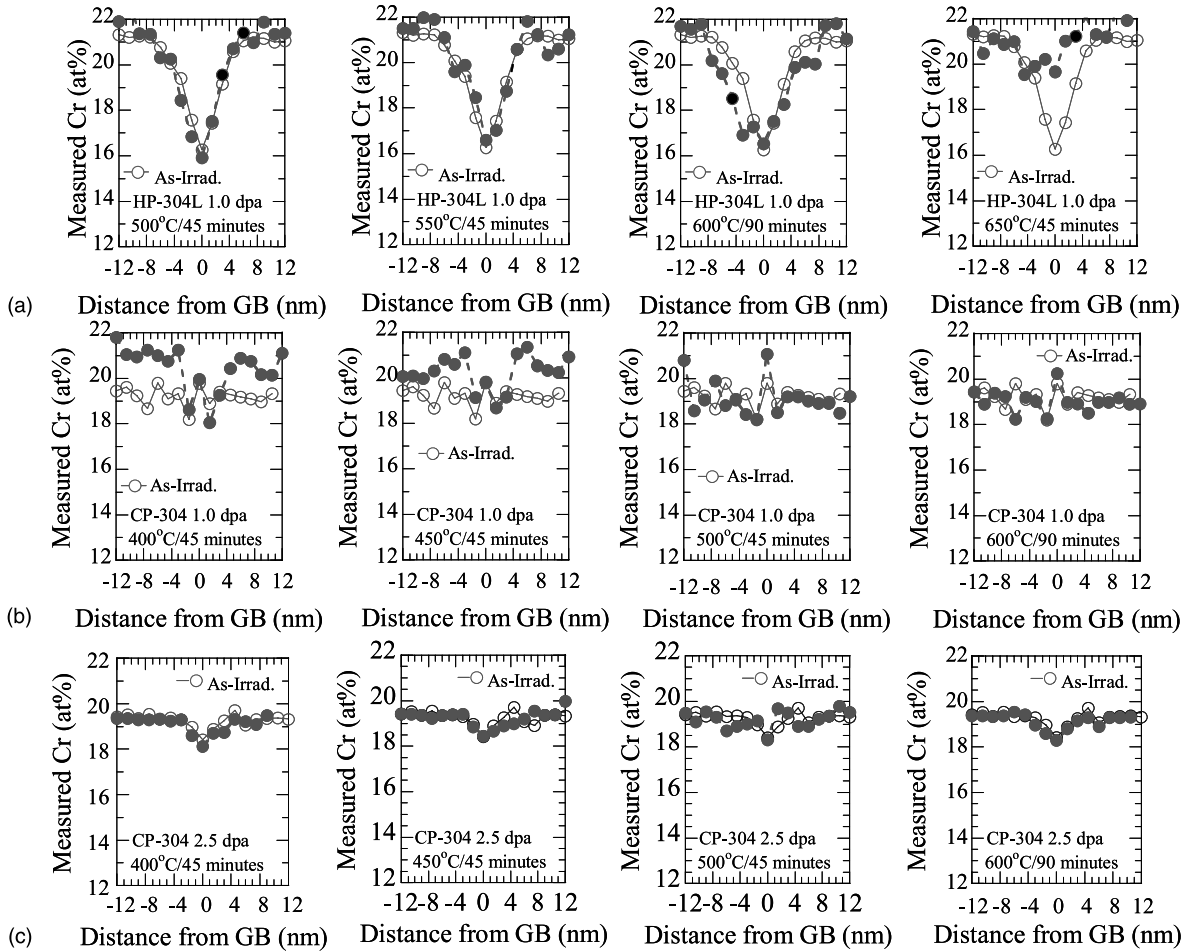
Fig. 5. Cr segregation profiles for HP-304L and CP-304 irradiated with 3.2 MeV protons at 360 °C to 1.0 and 2.5 dpa and post-irradiation annealed. The as-irradiated profile (open symbols) is shown in each figure. The 0 nm position is the grain boundary for all profiles.

at 600 °C/90 min. Grain boundary P also changed drastically during post-irradiation annealing. Following annealing at 400 °C for 45 min, the grain boundary P content dropped to 0.46 at.% from 1.47 at.% in the as-irradiated condition. All other treatments resulted in grain boundary P contents near the bulk level of 0.055 at.%.

The removal of Cr segregation for the HP-304L and CP-304 irradiated to 1.0 and 2.5 dpa is plotted in Fig. 6 as a function of Fe-diffusion distance. Because both time and temperature were varied, the diffusion distance of Fe was chosen as a single variable which combines both time and temperature effects. The diffusion distance is equal to $(D_{Fe}t)^{1/2}$ where t is annealing time and D_{Fe} is diffusivity for Fe at the annealing temperature. Also plotted in Fig. 6 are the results from experimental studies of Jacobs et al. [6], Katsura et al. [19], and Bruemmer et al. [20] for CP-304 and 316 irradiated to

~1.0 dpa. For alloys and doses where a 'w-shape' profile was observed, the percent of the minimum measured value remaining is plotted. Note that for conditions where the amount of Cr segregation *increased* with annealing, the percentage remaining is plotted as 100%. This is most significant in the data of Bruemmer where a CP-316 alloy with an extremely sharp 'w-shape' profile was measured. The Cr content measured in the as-irradiated case was above the bulk level and continued to increase above the bulk level during post-irradiation annealing. Overall, the data from this study and other studies are in excellent agreement. Only two annealing conditions (HP-304L at 650 °C/45 min and Katsura's CP-316 at 650 °C/1 h) resulted in the Cr segregation being less than 80% of the as-irradiated value.

In Fig. 7, the experimental data are compared to the predictions of the MIK model. The model predictions are plotted as a function of the measured results from

Table 3
Summary of grain boundary composition measurements[a] on post-irradiation annealed CP-304 (irradiated to 1.0 and 2.5 dpa at 360 °C)

Irradiation condition	Fe[a]	Cr[a]	Ni	P	Mo[a]	Mn	Si
CP-304 matrix/bulk composition	69.4	19.3	7.9	0.055	0.21	1.40	1.27
As-irradiated 1.0 dpa							
GB average (50 measurements)	66.7/68.2	19.6/18.5	8.6	1.47	0.41/0.22	1.09	2.14
Standard deviation of mean (at.%)	0.2/0.2	0.1/0.1	0.1	0.01	0.02/0.02	0.05	0.02
400 °C/45 min							
GB average (10 measurements)	67.9/68.9	19.8/18.6	8.7	0.08	0.41/0.35	1.27	1.85
Standard deviation of mean (at.%)	0.5/0.5	0.3/0.3	0.2	0.01	0.1	0.11	0.05
450 °C/45 min							
GB average (20 measurements)	67.9/69.1	20.2/18.6	8.5	0.07	0.27/0.27	1.18	1.79
Standard deviation of mean (at.%)	0.3/0.3	0.3/0.3	0.2	0.01	0.01	0.11	0.05
500 °C/45 min							
GB average (21 measurements)	67.4/69.5	20.9/18.9	8.5	0.07	0.27/0.23	1.17	1.67
Standard deviation of mean (at.%)	0.3/0.3	0.2/0.2	0.1	0.01	0.02/0.02	0.02	0.05
600 °C/90 min							
GB average (10 measurements)	67.9/69.2	20.3/18.8	8.9	0.06	0.22/0.22	1.13	1.47
Standard deviation of mean (at.%)	0.2/0.2	0.1/0.1	0.2	0.01	0.01/0.01	0.07	0.06
As-irradiated 2.5 dpa							
GB average (20 measurements)	66.8	18.4	9.7	1.47	0.35	0.85	2.42
Standard deviation of mean (at.%)	0.2	0.2	0.2	0.03	0.03	0.05	0.05
400 °C/45 min							
GB average (10 measurements)	68.0	18.3	9.9	0.46	0.33	1.00	2.02
Standard deviation of mean (at.%)	0.3	0.1	0.2	0.01	0.1	0.04	0.05
450 °C/45 min							
GB average (13 measurements)	68.2	18.4	9.7	0.08	0.31	0.82	1.95
Standard deviation of mean (at.%)	0.5	0.1	0.3	0.01	0.05	0.05	0.07
500 °C/45 min							
GB average (21 measurements)	68.8	18.4	9.8	0.07	0.25	0.83	1.77
Standard deviation of mean (at.%)	0.3	0.1	0.2	0.01	0.01	0.03	0.05
600 °C/90 min							
GB average (14 measurements)	68.8	18.3	9.7	0.07	0.22	0.91	1.57
Standard deviation of mean (at.%)	0.4	0.1	0.3	0.02	0.02	0.06	0.08

All results are listed in at.%.
[a] Average at GB/max (min) segregation measured adjacent to boundary for 'w-shaped' profiles.

both this study and available literature data. When plotted in this fashion, model and measured results can be compared for all available data. A line with a slope of unity was applied to the data set (shown in Fig. 7), resulting in a correlation coefficient of 0.85. A line with slope = 1 represents a one-to-one correlation between modeled and measured results. However, the most significant differences between the simulation and measured data occur where the measurements show no change in the as-irradiated Cr depletion. For these data points the model clearly overpredicts the rate of annealing. The majority of these data points are for conditions containing 'w-shape' profiles (CP-304 at 1.0 dpa and CP-316 data from Bruemmer), which the MIK model is not capable of simulating accurately [21]. Excluding these points from the statistical analysis improves the correlation coefficient to 0.93.

Grain boundary segregation of Si and P is removed much faster than Cr or Ni for the same annealing treatments. For both the 1.0 and 2.5 dpa CP-304 samples, the as-irradiated enrichment of Si and P are all significantly affected by annealing at 400 °C for 45 min, contrary to the observed annealing of Cr and Ni. The more rapid removal of Si segregation during post-irradiation annealing can be explained by considering the tracer impurity diffusion coefficients [22]. Silicon diffuses considerably faster than Cr or Ni. Coupled with a considerable Si enrichment in the 1.0 and 2.5 dpa condition
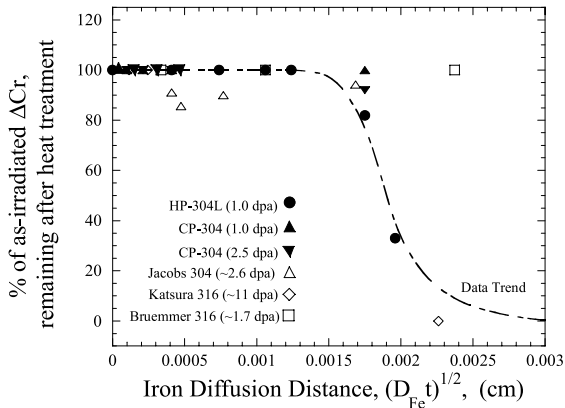
Fig. 6. Annealing of Cr segregation as a function of Fe-diffusion distance. The percentage of as-irradiated *minimum* measured Cr remaining is plotted for all conditions. Data points for CP-304 at 1.0 and 2.5 dpa have been shifted left and right, respectively, for clarity.
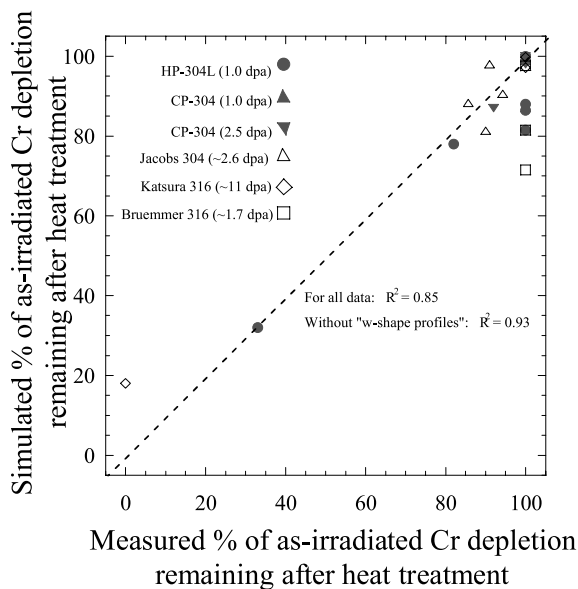

Fig. 7. Comparison of measured annealing of Cr segregation with annealing simulated using the MIK model.

(1.7 and 1.9 times bulk content, respectively), Si enrichment should be removed rapidly during post-irradiation annealing. Phosphorous also diffuses via vacancies in Fe–Cr–Ni alloys [23], although the diffusion coefficients are less well known than those for the major and other minor alloying elements. Nonetheless, in the as-irradiated 1.0 and 2.5 dpa condition, P is enriched a factor of 27 times over the bulk content (1.47 at.% for both 1.0 and 2.5 dpa versus a bulk content of 0.055 at.%). The extreme concentration gradient in the as-

irradiated condition can explain the very rapid removal of P enrichment during post-irradiation annealing.

4.2. Post-irradiation annealing of dislocation loops

During post-irradiation annealing, dramatic changes were measured in the dislocation loop population. For the HP-304L at 1.0 dpa and CP-304 at 1.0 and 2.5 dpa, the dislocation loop density decreased steadily with increasing annealing time or temperature while the mean dislocation size remained relatively unchanged. The mean loop diameters and loop densities were determined for each annealing condition and are summarized in Table 4 for both alloys. Bright field images of the dislocation population before and after annealing are shown in Fig. 8.

4.2.1. HP-304L

For the HP-304L, in the as-irradiated condition, the mean loop diameter was 11.0 nm. Annealing at 500 °C for 45 min resulted in a slightly smaller mean diameter (10.8 nm) while anneals at 600 °C for 45 min, and 600 °C for 90 min both resulted in a slightly larger loop diameter (11.7 and 12.1 nm, respectively). Bright field images of the dislocation loops in both the as-irradiated and annealed conditions are shown in Fig. 8(a). Some dislocation loops that have unfaulted and grown (not discriminated by the bright field imaging) may have contributed to this measured growth. Also, the simulations predicted the preferential removal of small loops from the population which would also result in an apparent growth in mean loop diameter. Alternatively, a portion of the dislocation loop population may, indeed, be composed of vacancy-type dislocation loops, that will grow with annealing. Computer simulation of the post-irradiation annealing of both vacancy and interstitial type dislocation loops by Simonen et al. [24] suggests that both the presence of vacancy-type loops in a loop population and their growth during annealing are feasible. Only annealing at 650 °C/45 min resulted in a loop size significantly smaller (9.2 nm) than the as-irradiated value. Contrary to the mean loop diameter, the dislocation loop density dropped significantly during annealing. In the as-irradiated condition, a loop density of 5.6×10^{21} m^{-3} was measured, which was steadily reduced with annealing. Following the most severe annealing condition (650 °C for 45 min) a density of only 0.14×10^{21} m^{-3} remained.

4.2.2. CP-304

For the CP-304 irradiated to 1.0 dpa and annealed, the very dense dislocation population in the as-irradiated condition is steadily reduced with annealing, as indicated in the bright field images shown in Fig. 8(b). In the as-irradiated condition, the mean loop diameter was 4.9 nm at a density of 17.0×10^{21} m^{-3}. During anneal-

Table 4
Summary of dislocation loop analysis on post-irradiation annealed HP-304L and CP-304 (irradiated to 1.0 and 2.5 dpa at 360 °C)

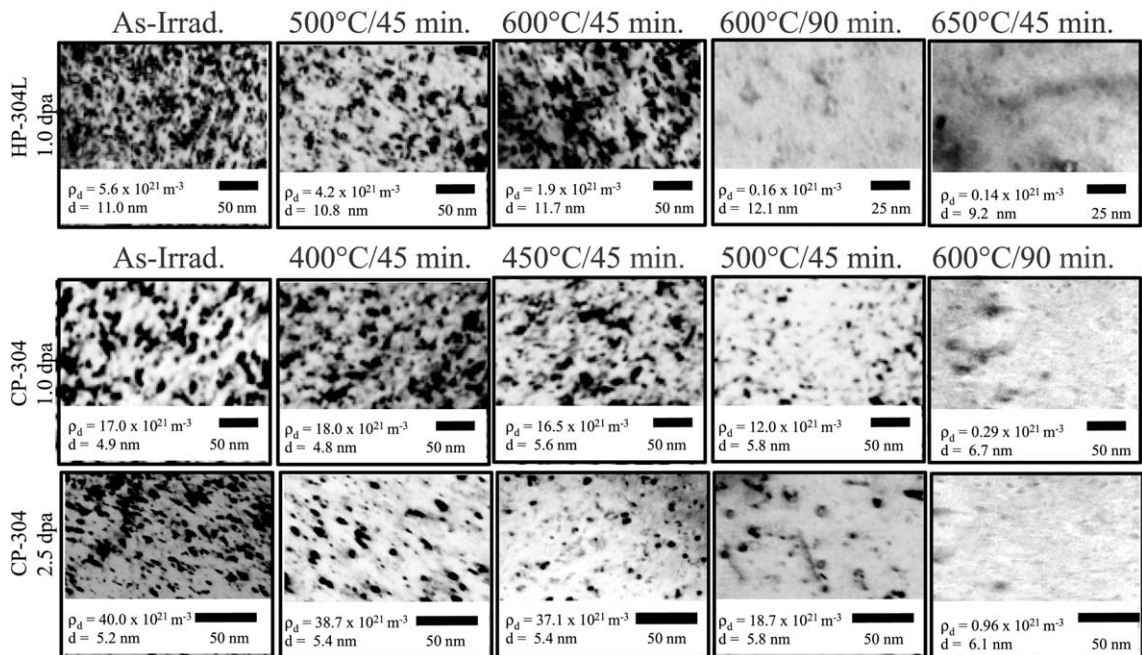| Annealing temperature (°C)	Annealing time (min)	Mean loop diameter (nm)	Loop density $\times 10^{21}$ (#/m^3)	Total loop line length $\times 10^{14}$ (m/m^3)	As-irradiated line length remaining (%)
HP-304L 1.0 dpa					
As-irradiated		11.0	5.6	1.94	100.0
500	45	10.8	4.2	1.43	73.6
600	45	11.7	1.9	0.69	36.1
600	90	12.1	0.16	0.06	3.1
650	45	9.2	0.14	0.04	2.1
CP-304 1.0 dpa					
As-irradiated		4.9	17.0	2.61	100.0
400	45	4.8	18.0	2.71	100.0
450	45	5.6	16.5	2.90	100.0
500	45	5.8	12.0	2.19	83.8
600	90	6.7	0.29	0.06	2.4
CP-304 2.5 dpa					
As-irradiated		5.2	40.0	6.53	100.0
400	45	5.4	38.7	6.56	100.0
450	45	5.4	37.1	6.29	96.4
500	45	5.8	18.7	3.41	52.2
600	90	6.1	0.96	0.18	2.8

Fig. 8. Bright field images of dislocation loop populations in HP-304L and CP-304 irradiated with 3.2 MeV protons at 360 °C to 1.0 and 2.5 dpa and post-irradiation annealed.

ing, the mean loop diameter increased slightly (up to 6.7 nm after 600 °C/90 min). The dislocation loop density steadily decreased with increased annealing time or temperature. Following annealing at 600 °C for 90 min, very few loops were observed.

Bright field images of the dislocation population following proton irradiation of the CP-304 to 2.5 dpa and subsequent annealing are also shown in Fig. 8. As in the samples irradiated to 1.0 dpa, the very dense dislocation population in the as-irradiated condition is
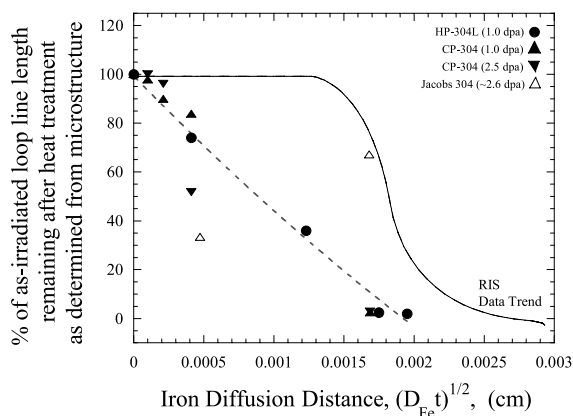
Fig. 9. Annealing of dislocation microstructure as a function of Fe-diffusion distance. The fraction of the as-irradiated loop line length associated with the dislocation population remaining is plotted.

Fig. 10. Comparison of simulated and measured annealing of dislocation loop line length.

steadily removed with annealing. The mean loop size grew from the as-irradiated diameter of 5.2 nm to 6.1 nm following annealing a 600 °C/90 min anneal. Loop density dropped from the as-irradiated density of 40.0×10^{21} m^{-3} to 0.96×10^{21} m^{-3} after the same 600 °C/90 min anneal.

The behavior of the dislocation microstructure during post-irradiation annealing of the CP-304 alloy in this study is summarized in Fig. 9. Also plotted are the results for neutron-irradiated 304SS by Jacobs et al. [6]. The total dislocation line length associated with the dislocation loop population is plotted as a function of Fe-diffusion distance. The loop line length from the proton-irradiated samples is removed steadily with increasing annealing time or temperature. Jacob's data, however, are somewhat contradictory. The two data points from the neutron-irradiated samples indicate that the line length actually increases during annealing. Jacobs measured a large increase in loop diameter (6.7 to 10.7 nm) for the anneal at a diffusion distance of 0.0017 cm (475 °C for 24 h) and attributed this discrepancy to the unfaulting of dislocation loops which artificially increased the mean loop diameter.

The experimental data of both this study and that of Jacobs are compared to the dislocation loop-annealing model in Fig. 10. The simulated results are plotted as a function of measured results for each experimental data point in this study and available data from other studies. A line with a slope of one is also plotted in Fig. 10. This line fits the data set with a correlation coefficient of 0.92. As with the comparison of RIS annealing shown in Fig. 7, there is no systematic difference between measured and model results.

However, comparison of the measured loop sizes with the simulated results reveals a discrepancy. The loop
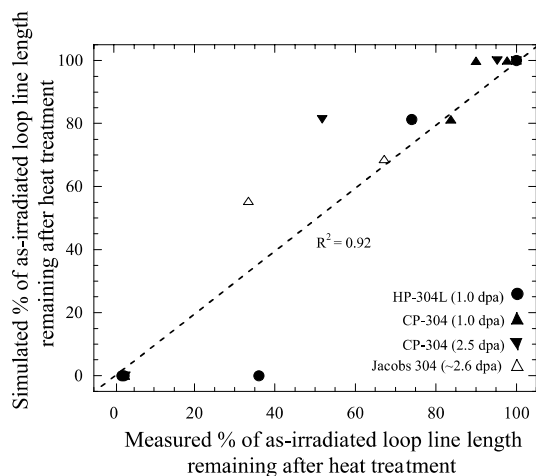
annealing model predicts that the mean loop size will shrink steadily during annealing while experimental results show that the loop size remains constant or increases slightly during annealing up to anneals at 600 °C for 90 min, beyond which the loop radius decreases. Thus, in order for the simulated change in yield stress to match the experimental values, the model must underpredict the change in loop density to compensate for the overprediction of change in loop radius. This discrepancy may be explained by the unfaulting of dislocation loops during annealing, as noted by Jacobs. Dislocation loops that unfault are free to grow or glide and will behave differently during post-irradiation annealing. According to Olander [25], unfaulting is very slow at temperatures below ~550 °C, but dislocation loops may spontaneously unfault at temperatures above 600 °C. Since the bright field imaging technique used in this study images both faulted and unfaulted dislocation loops, the reported diameter and density may have been determined from a population containing some unfaulted dislocation loops, similar to the experience of Jacobs. The dark field rel-rod technique images only faulted dislocation loops and could resolve this issue. However, the rel-rod technique is extremely hard to use to image very low dislocation densities, which is why the bright field technique was used exclusively in this study.

4.3. Annealing of hardness

As with dislocation loop density, the measured hardness decreased steadily with increasing annealing time or temperature for both the HP-304L and the CP-304 (at both 1.0 and 2.5 dpa). Table 5 lists the results of the hardness measurements for both the as-irradiated and annealed specimens. For the HP-304L alloy irradi-

Table 5
Summary of hardness analysis on post-irradiation annealed HP-304L and CP-304 (irradiated to 1.0 and 2.5 dpa at 360 °C)

Anneal temperature (°C)	Anneal time (min)	Unirradiated H_v (kg/mm²)	As-irradiated H_v (kg/mm²)	As-irradiated ΔH_v (kg/mm²)	Annealed H_v (kg/mm²)	Annealed ΔH_v (kg/mm²)	From hardness		From loops	
							$\Delta\sigma_y$ (MPa)	As-irradiated $\Delta\sigma_y$ remain (%)	$\Delta\sigma_y$ (MPa)	% As-irradiated $\Delta\sigma_y$ remain
HP-304L 1.0 dpa										
As-irradiated		167	229	62	229	62	219.8	100.0	186.2	100.0
500	45	167	223	56	212	45	159.6	72.5	159.8	85.8
500	300	167	234	67	207	40	141.8	59.7	–	–
550	45	167	234	67	217	50	177.3	74.6	–	–
600	45	167	224	57	182	15	53.2	24.2	111.8	60.1
600	90	167	250	83	166	−1	−3.5	−1.2	33.0	17.7
650	45	167	255	88	156	−11	−39.0	−12.5	26.9	14.5
CP-304 1.0 dpa										
As-irradiated		220	270.5	50.5	270.5	50.5	179.1	100.0	227.5	100.0
400	45	220	270.5	50.5	273.0	53.0	187.9	105.0	223.4	98.2
450	45	220	270.5	50.5	273.7	53.7	190.4	106.3	215.9	94.9
500	45	220	270.5	50.5	266.4	46.4	164.5	91.9	207.9	91.4
600	90	220	270.5	50.5	228.8	8.8	31.2	17.4	36.8	16.2
650	45	220	270.5	50.5	218.9	−1.1	3.9	−2.2	–	–
CP-304 2.5 dpa										
As-irradiated		220	326.0	106.0	326.0	106.0	375.9	100.0	359.5	100.0
400	45	220	326.0	106.0	320.8	100.8	357.4	95.1	360.1	100.0
450	45	220	326.0	106.0	316.1	96.1	340.8	90.6	352.6	98.0
500	45	220	326.0	106.0	290.8	70.8	251.1	66.8	259.9	72.0
600	90	220	326.0	106.0	234.3	13.4	47.5	12.6	60.0	16.7

ated to 1.0 dpa, a hardness of 229 kg/mm² (62 kg/mm² above the unirradiated value) was measured. After annealing at 500 °C for 45 min, hardness was reduced to 212 kg/mm² (a 28.5% reduction in radiation-induced hardness). Increased annealing temperature resulted in an increased removal of radiation-induced hardening. After annealing at 600 °C/90 min or 650 °C/45 min all radiation-induced hardening was removed.

For the CP-304 alloy in the 1.0 dpa as-irradiated condition, a hardness of 271 kg/mm² (51 kg/mm² above the unirradiated value of 220 kg/mm²) was measured by Was et al. [1] and confirmed in this study. After annealing at 400 and 450 °C/45 min, the hardness remained at the as-irradiated level. However, annealing at 600 °C/90 min removed almost all the as-irradiated hardness increase. Similarly, for the 2.5 dpa samples, after annealing at 400 °C/45 min and at 450 °C/45 min the hardness was not significantly different from the as-irradiated level, while annealing at 600 °C/90 min removed a more significant portion of the radiation-induced hardening (only 16.7% remaining).

The fraction of radiation-induced yield stress change calculated from hardness measurements is plotted as a function of Fe-diffusion distance in Fig. 11 for both the CP-304 irradiated to 1.0 and 2.5 dpa and the HP-304L of this study. The results from studies by Jacobs, Asano,
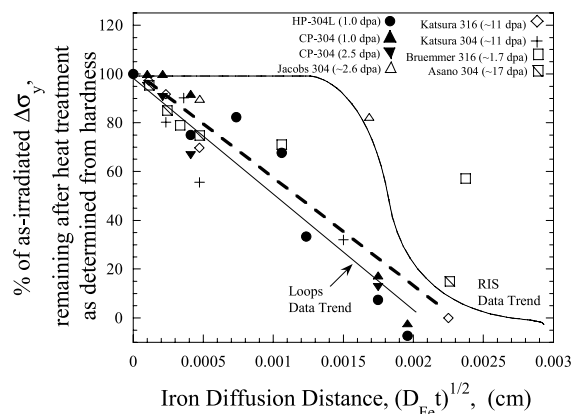

Fig. 11. Annealing of measured hardness as a function of Fe-diffusion distance. The remaining fraction of the as-irradiated change in yield stress calculated from hardness measurements is plotted.

Bruemmer, and Katsura on 304 SS and Katsura on 316 SS are also plotted. With the exception of single data points from Bruemmer and Jacobs each, the hardness decreases steadily with increasing annealing time and temperature for all alloys. Further, the data from this study are in excellent agreement with that from Jacobs

[6], Katsura [19], and Bruemmer [20]. However, more importantly, all the data from hardness measurements follow the same trend during annealing and are also in excellent agreement with that calculated from micro-structure measurements.

4.4. IASCC of post-irradiation annealed stainless steel

The strain-to-failure and extent of IG cracking changed dramatically during post-irradiation annealing for both 1.0 and 2.5 dpa CP-304 samples tested in the NWC environment. The strain-to-failure and measured ultimate tensile strength (UTS), as well as the location and nature of failure for each specimen in CERT tests of the 1.0 and 2.5 dpa samples are summarized in Table 6. With annealing, the strain-to-failure increased with increasing diffusion distance for both 1.0 and 2.5 dpa samples. The 1.0 dpa sample annealed at 400 °C for 45 min failed at 23.3%, close to the strain-to-failure of the as-irradiated specimens, while all other annealed 1.0 dpa samples failed at ∼30% strain, which is more representative of the 0.3 dpa samples of the same alloy which failed via ductile rupture [1]. Similarly, the strain-to-failure for the 2.5 dpa sample annealed at 400 °C for 45 min was 26.5% while the sample annealed at 500 °C for 45 min failed at 33.7% strain. All four 1.0 dpa specimens failed in the unirradiated region or the threads of the sample. All faces of each specimen and the fractured ends were examined in detail for evidence of IG cracking. The 1.0 dpa samples annealed at 400 and 450 °C for

45 min both had one crack on the irradiated face of the specimen, approximately 250 μm long and IG in nature. This is approximately the same length of IG cracking observed on the fractured end in the 1.0 dpa as-irradiated specimens strained under the same conditions [1]. For the samples annealed at 500 °C/45 min and the 600 °C/90 min, no cracks were found on any of the sample surfaces. All four of the post-irradiation annealed 2.5 dpa samples failed in the irradiated region. The samples annealed at 400 and 450 °C for 45 min both exhibit a fracture morphology similar to the 3.0 dpa as-irradiated fracture morphology. In addition to the crack leading to failure, 2 and 6 additional cracks were found on the irradiated surface for the samples annealed at 400 and 450 °C, respectively. Contrary to the samples annealed at 400 °C and 450 °C for 45 min, the sample annealed at 500 °C/45 min failed entirely via ductile rupture. Finally, the 2.5 dpa sample annealed at 600 °C/90 min exhibited extensive IG cracking on all four faces of the sample, not just the irradiated face, similar to that observed in sensitized specimens. Cookson [26] tested a sensitized HP-304L sample (650 °C for 24 h) under identical water conditions and observed almost 100% IG failure at only 11.5% strain (compared to 30% strain-to-failure for unirradiated specimens), suggesting that the 2.5 dpa sample may have actually been annealed at temperature higher than 600 °C and sensitized (potentially due to a thermocouple failure).

The percentage of as-irradiated crack length remaining after post-irradiation annealing is plotted in

Table 6
Summary of CERT test results performed on post-irradiation annealed CP-304 samples (1.0 and 2.5 dpa)

Annealing temperature (°C)	Annealing time (min)	Strain at failure (%)	UTS (ksi)	Location of failure	Number of cracks in irradiated region	Total crack length on irradiated surface (μm)[a]
CP-304 1.0 dpa						
400	45	23.3[b]	62.1[c]	Unirradiated region	1	270
450	45	30.0[b]	NA	Unirradiated region	1	234
500	45	30.6	66.6	Threads	0	0
600	90	30.6	75.8	Near shoulder	0	0
CP-304 2.5 dpa						
400	45	26.5	60.3	Irradiated region	3	1540
450	45	22.7	59.1	Irradiated region	7	3540
500	45	33.7	64.0	Irradiated region	0	0
600	90	10.8	40.5	Irradiated region	0	0

[a] Sum of length of all regions characterized as IG or TG, including crack that led to failure.
[b] Estimated due to load cell failure prior to sample failure ±0.5%.
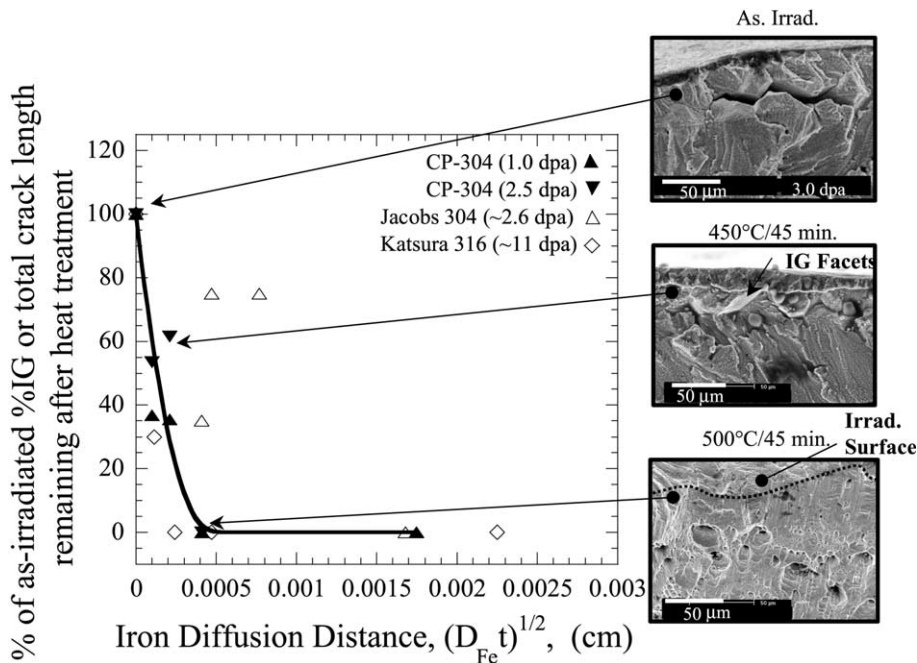[c] Maximum measured before load cell failed.

Fig. 12. Comparison of measured total crack length or %IG remaining as a function of Fe-diffusion distance. Also, the irradiated surface of CP-304-2.5 dpa sample post-irradiation annealed at 450 and 500 °C for 45 min are shown. Samples strained at 3×10^{-7} s^{-1} in water at 288 °C, 0.2 µS/cm and 2 ppm O$_2$. A line has been added to the fracture surface of the sample annealed at 500 °C for 45 min to indicate the irradiated surface of the sample.

Fig. 12. Even the lowest temperature anneal reduced the crack length relative to the as-irradiated level. Annealing at 500 °C for 45 min and above removed all evidence of IG cracking in both the 1.0 and 2.5 dpa samples. The rapid and distinct change in cracking mode from clearly IG after annealing at 450 °C to completely ductile after annealing at 500 °C is also shown in Fig. 12. The cracking results of this study are in good agreement with the cracking response measured by Jacobs [6] and Katsura [19] on neutron-irradiated and annealed 304 and 316 stainless steels, respectively.

5. Discussion

Simulations predicted that dislocation loops were removed preferentially over RIS. Comparison of the measured and simulated annealing confirmed the accuracy of the simulations for both segregation profiles and dislocation loops. The experimental separation of loops and RIS via post-irradiation annealing is confirmed in the following section. The effects of Cr, Si and P segregation in IASCC are then examined by comparing the behavior of cracking and RIS during annealing. In a similar manner, the importance of dislocation loops and hardness in IASCC are determined.

5.1. Separation of RIS and loops

The effects of post-irradiation annealing on micro-chemical changes were considerably different than those on microstructure and hardening. Very little change was observed in grain boundary composition or composition profiles in either alloy at most annealing conditions examined. Even under the most extreme conditions (600 °C for 90 min) RIS was largely unchanged. For all other conditions examined up to 600 °C/90 min, measured microchemistry was virtually identical to the as-irradiated condition. Significant changes in loop population and hardness were observed following post-irradiation annealing, in contrast to the behavior observed for RIS. The data trends for the removal of RIS (Fig. 6) and dislocation microstructure (Fig. 9) are superimposed over the annealing of hardness shown in Fig. 11. The removal of dislocation loops and hardness follow the same trend and both are clearly removed preferentially to RIS. Indeed, annealing at 600 °C for 90 min removed virtually all radiation-induced changes to yield stress. The preferential removal of dislocation loops and hardening is consistent with the annealing simulations. Further, RIS is not affected until 80% of the dislocation microstructure or hardening has been removed, which is consistent with the simulations discussed in Section 2.2.2

and shown in Fig. 4 and supports that the preferential removal of dislocation loops is partially due to competition for vacancies between the removal of RIS and loops.

In summary, measured results from both this study and other studies indicate that dislocation loops were removed preferentially over RIS. Comparison of the measured and simulated annealing confirmed both the accuracy of the simulations and the preferential removal of the dislocation loop microstructure during annealing. Since microchemical changes were separated from microstructural changes and hardening, the cracking susceptibility following annealing was compared to the as-irradiated condition. Although the cracking susceptibility was removed before RIS was truly isolated from the dislocation loops or hardening, careful comparison of the annealing behavior of both cracking and RIS may help to assess the importance of RIS in IASCC. Direct comparisons of as-irradiated and annealed cracking susceptibility to as-irradiated and annealed dislocation loop microstructure and hardening provide further insight into the effect of each irradiation-induced change on IASCC.

5.2. RIS of Cr and Ni and IASCC

As shown in Fig. 13(a), the grain boundary Cr and Ni contents remain at the as-irradiated level over the range of annealing conditions (plotted as a function of Fe-diffusion distance) for both 1.0 and 2.5 dpa samples. However, IG cracking susceptibility clearly shows a very rapid decrease with increasing annealing time or temperature and is completely eliminated after annealing at 500 °C for 45 min.

Given that the IG cracking susceptibility was removed before the grain boundary Cr content begins to change indicates that Cr depletion alone cannot be a primary contributor to IASCC. This result is consistent with the observed difference in cracking behavior of proton-irradiated CP-304 and the companion CP-316 alloy studied previously [1]. At all doses, the CP-316 exhibited more Cr depletion (in 'w-shape' at 1.0 dpa or in 'v-shape' at higher damage levels) than the CP-304 alloy, yet the CP-316 alloy did not crack at doses up to 5.0 dpa. Jacobs [27] also concluded in his study of neutron-irradiated 304 SS that "the depletion of Cr does not appear to be a primary causative factor in IASCC".
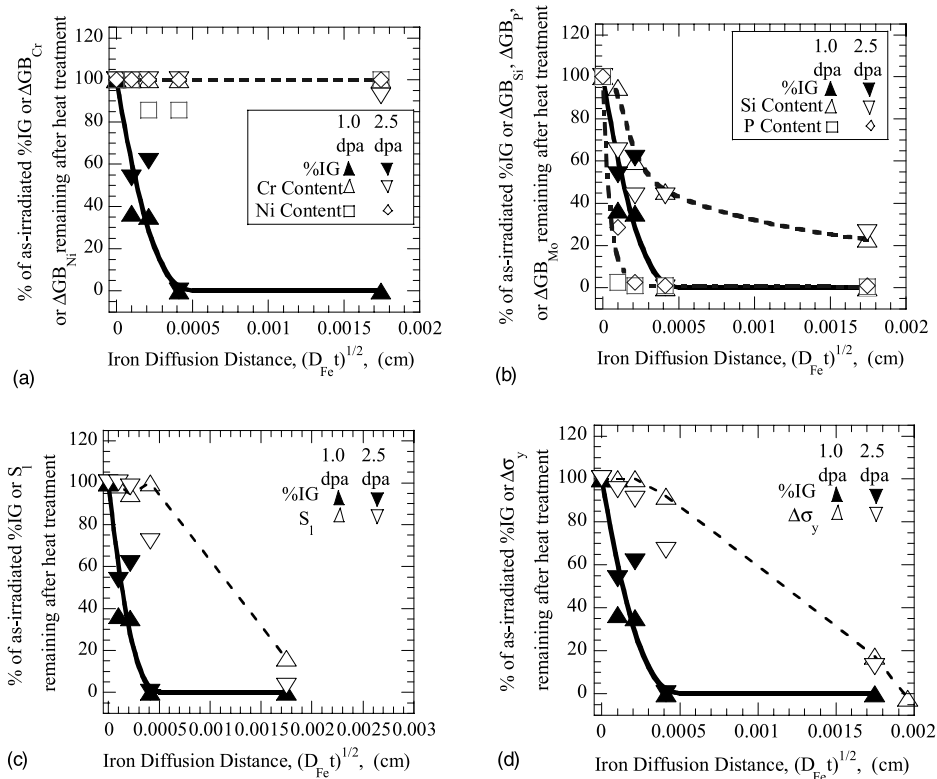

Fig. 13. Comparison of annealing behavior of major alloying elements (a), minor alloying elements (b), dislocation loop line length (c) and hardness (d) with cracking susceptibility for CP-304 irradiated to 1.0 and 2.5 dpa.

Similarly, the grain boundary enrichment of Ni does not play an important role in the mitigation of IASCC as cracking was removed during annealing with no measurable change in Ni segregation. As shown earlier in Fig. 1, grain boundary Ni content steadily increases with dose and is approximately twice the bulk level by 5.0 dpa. However, cracking susceptibility also increases steadily with increasing dose through 5.0 dpa, reinforcing that Ni enrichment cannot be a mitigating factor for IASCC.

5.3. RIS of Si and P and IASCC

Silicon and phosphorus enrichment and cracking susceptibility are compared in Fig. 13(b). During annealing, both Si and P enrichment are removed rapidly, at a rate similar to that of cracking susceptibility. The similarities in recovery rates of both Si and P enrichment to that of the cracking susceptibility potentially implicates both elements as contributors to IASCC.

However, substantial literature data suggest that Si plays a beneficial role, if any at all [26–31]. Chung [28] and Fukuya [29] both found that CP alloys with higher Si content were less susceptible to IG cracking than high purity alloys irradiated to the same conditions. Tsukada [30] reported that an alloy with high Si content failed at a higher strain than a high purity reference alloy with a comparable fraction of IG cracking. Only Jacobs et al. [31] reported any potential link between cracking and Si content. However, in a later study, Jacobs [27] reported grain boundary Si enrichment had little impact on IASCC. Finally, the work of Cookson [26] showed that increased Si content had a slightly beneficial effect on cracking of proton-irradiated HP-304 SS. Combined, the experimental evidence from other studies shows that the role of Si segregation in IASCC is minor.

The grain boundary P content of both 1.0 and 2.5 dpa samples, returned to the bulk content following even the shortest anneal (400 °C for 45 min), faster than the mitigation of cracking. Fig. 1(b)) plotted the dose dependence of grain boundary P and cracking susceptibility for the CP-304 SS alloy. While the percentage of IG cracking increases steadily with dose, the grain boundary P content increased dramatically between 0.3 and 1.0 dpa. Thereafter, the P content remained relatively unchanged until dropping back to the bulk level by 5.0 dpa (while cracking susceptibility continued to increase). The trends during annealing and dose dependence reveal that P enrichment during irradiation is not the primary cause of IASCC, consistent with the work of Cookson [26], Fukuya et al. [29], Tsukada et al. [30], Chung et al. [32], and Jacobs [33] who all reported that P had either no effect or a slightly beneficial effect. While the results of this study indicate that the effects of minor alloying elements such as Si and P on IASCC to be minor, other minor alloying elements and impurities such as C, B or N may be influential in IASCC.

5.4. Dislocation loops and IASCC

The total loop line length calculated from the dislocation loop microstructure is compared to the cracking susceptibility in Fig. 13(c). During annealing, the cracking susceptibility was mitigated before the total loop line length was significantly changed. No changes in loop density or diameter were measured following annealing at 400 or 450 °C for 45 min. The lack of change in loop line length after annealing at 500 °C for 45 min may be due to the inclusion of unfaulted loops in the density count.

With irradiation (Fig. 1(c)), the total dislocation line length associated with dislocation loops increased quickly with dose, reaching a saturation level between 1.0 and 3.0 dpa with little increase between 3.0 and 5.0 dpa. The cracking susceptibility, however, continued to increase considerably between 3.0 and 5.0 dpa. Further, dislocation densities and diameters measured in the proton-irradiated CP-316 SS alloy were similar to those measured in the CP-304 alloy [1]. Despite the similar loop populations, a distinct difference in cracking susceptibility exists. Therefore, the observed dislocation microstructure alone is not the primary mechanism for IASCC.

5.5. Hardness and IASCC

The impact of radiation-induced hardening is assessed in Fig. 13(d), which plots the change in yield stress and IG cracking susceptibility as a function of diffusion distance. During annealing of both 1.0 and 2.5 dpa specimens, the degree of hardening remains at the as-irradiated level for anneals at 400 and 450 °C. The hardening recovers slightly after annealing at 500 °C for 45 min, while cracking has been completely removed, indicating that cracking susceptibility is not determined by hardness alone.

Like the dislocation loop microstructure, the change in yield stress increases steadily with increasing radiation dose up to 3.0 dpa. Between 3.0 and 5.0 dpa, there is little increase in yield stress change. Further, hardening of the proton-irradiated CP-316 alloy were similar to those measured in the CP-304 of this study in spite of the difference in cracking behavior [1]. Thus, radiation-hardening alone cannot explain the occurrence of IASCC in the alloys examined.

5.6. Other potential contributors to IASCC

The segregation of Cr, Ni, Si and P were each found to be insufficient to cause IASCC alone. Further, the

dislocation microstructure and radiation-induced hardening alone did not correlate with IASCC. All of these effects may contribute to IASCC; however, none seems to be sufficient to cause IASCC alone. Therefore, some other feature or radiation-induced change must be controlling the observed IASCC behavior. Possibilities include the segregation of other minor elements such as B, C or N, which are not typically measured, unresolved small defect clusters, or a combination of effects.

5.6.1. Other elements

The CP-304 alloy contains minor elements such as B, C and N, which were not analyzed in this study. Quantitative analysis via STEM/EDS of B, C, or N is extremely difficult due to the low X-ray yields of these light elements. Further, significant peak overlap with lower energy peaks of major alloying elements such as Fe, Cr and Ni makes even qualitative analysis difficult. The CP-304 and CP-316 studied by Was et al. [1] have similar levels of C (0.16 and 0.18 at.%, respectively) and N (0.266 and 0.230 at.%, respectively), making it difficult to explain the difference in cracking susceptibility between the two alloys on the basis of these elements alone.

Boron has been identified as potentially having beneficial effects on IASCC [34]. Chung et al. [32] reported that higher B concentration was beneficial in suppressing IASCC. In a study by Jenssen et al. [12], alloys with low boron content showed higher susceptibility to IASCC than those with higher bulk B levels. Boron was measured by Kenik et al. [35] using atom probe analysis in both the unirradiated CP-304 and CP-316 alloys studied by Was [1]. The grain boundary B content in the CP-316 SS was measured at 4.4 at.%, considerably higher than the 1.4 at.% content measured in the CP-304 SS, consistent with the observations of Chung [28] and Jenssen [12] and supporting the potentially beneficial role of B. However, analysis of the grain boundary B content must be performed on irradiated samples to confirm any potential role of B in suppressing IASCC.

Other analytical techniques such as atom probe might be useful, however, techniques for creating atom-probe samples from proton-irradiated samples do not currently exist.

5.6.2. Small defect clusters

Fine scale radiation damage may also be a possible contributor to IASCC. During irradiation, interstitials or vacancies also survive the cascade event, either as individual defects or as small clusters. The small clusters may take the form of small vacancy or interstitial loops, stacking fault tetrahedra, di- or tri-vacancy clusters, interstitial clusters or defect-impurity clusters.

During deformation, these small defect clusters will act as obstacles to moving dislocations, similar to dislocation loops. Small defect structures are typically not characterized due to the extreme difficulty in imaging this type of damage. Further, techniques used to prepare TEM disks such as ion milling can induce small defect damage in metal samples, the amount of which is dependent upon material and, temperature, rate, and angle of ion milling [36].

During annealing, small defects may be removed quickly via annihilation due to their small size, or they may spontaneously dissociate, leaving interstitials or vacancies behind, as shown schematically in Fig. 14. Dislocation loops may absorb these free interstitials and the mean radius may slightly increase, as experimentally observed in both the CP-304 SS of this study and by Jacobs [6]. The increase in hardness due to an increase in loop size is offset by the removal of the small defect clusters resulting in no observable change in loop density. Hence, the net effect is a change in defect morphology with no discernible change in dislocation loop density or yield strength calculated from measured hardness.

Also note that the mitigation of cracking during post-irradiation annealing shown in Fig. 12 is very similar in this study and that of Jacobs and Katsura. The similarity in cracking mitigation, despite the wide disparity
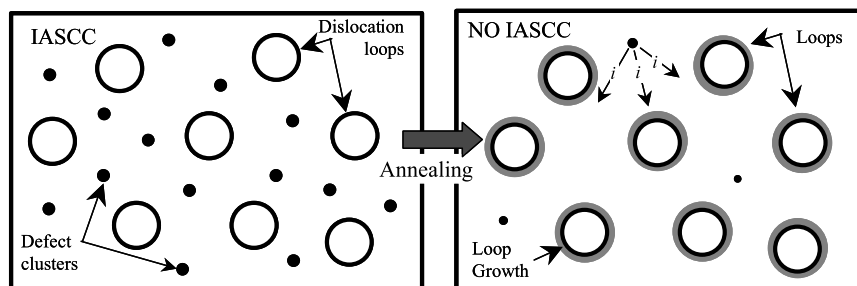

Fig. 14. Schematic of annealing behavior of mixed population of black-dot damage and dislocations. During annealing, small defect clusters are removed or dissociate into individual interstitials which may then be absorbed by dislocation loops. This process results in a population of larger loops with no apparent change in density.

in as-irradiated dose, indicates that cracking is controlled by a mechanism, which has reached a critical level by 1.0 dpa (since cracking was observed at this dose). The fine defect damage reaches a saturation level very quickly during irradiation [37]. The rapid removal of a dense population of small obstacles impeding dislocation motion could result in a drastic change in deformation mode and, hence, cracking behavior during annealing. This is consistent with the work of Bailat et al. [38] who reported a correlation between deformation mode and IASCC in neutron-irradiated stainless steels.

5.6.3. Combination of radiation-induced segregation and microstructure

RIS of any one element, the formation of dislocation loops or increases in hardness cannot alone account for the observed IASCC behavior. However, the presence of two or more effects at a critical level may be responsible, as suggested by Chung et al. [32]. The results of this study suggest that a combination of RIS, dislocation loops, and/or hardening controlling IASCC is unlikely. Considering that the cracking susceptibility was mitigated with even the shortest annealing treatment, prior to Cr or Ni segregation, dislocation loops, and hardening being altered, no combination of the effects examined in this study can be solely responsible. However, changes in both the dislocation loop population and hardness might occur at the same time and offset each other, as discussed previously.

6. Conclusions

The objective of this work was to determine the role of RIS in IASCC by using the measurement of grain boundary composition and post-irradiation annealing in a series of proton-irradiated alloys. Dislocation microstructure was removed preferentially during post-irradiation annealing. Further, RIS can be isolated from dislocation microstructure and hardening by annealing at 600 °C for 90 min. Simulations predicted that dislocation loops were removed preferentially over RIS. Comparison of the measured and simulated annealing confirmed both the accuracy of the simulations and the preferential removal of dislocation microstructure during annealing.

Based upon comparison of as-irradiated and annealed specimens, RIS of Cr, Ni, Si or P is not sufficient to cause IASCC. Depletion of Cr during irradiation plays a secondary role in IASCC based upon the distinct difference in cracking and Cr depletion behavior during post-irradiation annealing. Likewise, Ni content remained constant during post-irradiation annealing while cracking was mitigated rapidly, indicating that Ni enrichment is not a mitigating factor for IASCC. The enrichment of Si at grain boundaries was shown to be non-controlling given the distinct difference in cracking behavior and Si content between the CP-304 in this study and the CP-316 alloy examined in a previous study. Finally, the enrichment of P has a minimal impact on IASCC based upon differences in development of P segregation and cracking during irradiation and during post-irradiation annealing.

Neither dislocation microstructure or radiation hardening are sufficient to induce IASCC alone. During annealing, the cracking was mitigated quickly while the total loop line length and measured hardness were not significantly changed with annealing at 400, 450 or 500 °C for 45 min. The hardness recovers only slightly after annealing at 500 °C for 45 min, while cracking has been completely mitigated, reducing the role of radiation-induced hardening in IASCC.

If none of the observed changes are solely responsible for the increase in cracking susceptibility with increasing dose (either alone or combined), some other feature or irradiation-induced change which cannot be easily characterized by TEM imaging or EDS analysis must be responsible. Boron has been identified in several studies as a potentially beneficial presence at grain boundaries; however, measuring B content is exceedingly difficult. While not directly measured, fine scale defects and their expected behavior during annealing make them a potential contributor to IASCC. During post-irradiation annealing, small interstitial clusters might be removed very quickly via vacancy absorption due to their small size and the high driving force for annihilation. The rapid removal of a dense population of small obstacles impeding dislocation motion could result in a drastic change in cracking behavior during annealing like that observed experimentally.

References

[1] G.S. Was, J.T. Busby, J. Gan, E.A. Kenik, A. Jenssen, S.M. Bruemmer, P.M. Scott, P.L. Andresen, J. Nucl. Mater. 300 (2002) 198.

[2] S.H. Song, R.G. Faulkner, P.E.J. Flewit, P. Marmy, M. Victoria, Mater. Sci. Eng. A A26 (2000) 230.

[3] M. Guttman, J. Phys. IV 5 (1995) 85.

[4] M. Guttmann, P. Dumoulin, M. Wayman, Metall. Trans. A 13A (1982) 1693.

[5] T.W. Xu, Scripta Metal. 37 (1997) 1643.

[6] A. Jacobs, in: Proceedings of the 7th Env. Deg, NACE International, Houston TX, 1995, p. 1021.

[7] A. Jacobs, G.E.C. Bell, C.M. Sheperd, G.P. Wozadlo, Corrosion 51 (10) (1995) 731.

[8] I.M. Kodama, N. Yokota, K. Asano, T. Kato, K. Fukuya, J. Nucl. Mater 239 (1996) 90.

[9] T.R. Allen, PhD Thesis, University of Michigan, 1995.

[10] B. Burton, Mater. Sci. Tech. 8 (1992) 602.

[11] Seeger, in: Proceedings of 2nd UN International Conference On Peaceful Uses of Atomic Energy, Geneva, vol. 6, September 1958, pp. 250.

[12] A. Jenssen, L.G. Ljungberg, in: Proceedings of Seventh International Symposium on Environmental Degradation of Materials in Nuclear Power Systems-Water Reactors, NACE International, Houston, TX, 1995, p. 1043.

[13] D.L. Damcott, J.M. Cookson, V.H. Rotberg, G.S. Was, Nucl. Instr. and Meth. B 99 (1995) 780.

[14] D.L. Damcott, J.M. Cookson, R.D. Carter Jr., J.R. Martin, M. Atzmon, G.S. Was, Radiat. Eff. Defect. Solid. 118 (1991) 383.

[15] T.R. Allen, D.L. Damcott, G.S. Was, E.A. Kenik, in: Proceedings of the 7th Environmental Degradation, NACE International, Houston, TX, 1995, p. 997.

[16] ASTM Designation E521-89, Annual Book of ASTM Standards, vol. 12.02, American Society for Testing and Materials, Philadelphia, PA, 1989, p. D-9.

[17] H.R. Higgy, F.H. Hammad, J. Nucl. Mater. 55 (1975) 177.

[18] P.L. Andresen, in: R.H. Jones (Ed.), Stress-Corrosion Cracking, Materials Performance and Evaluation, ASM International, Materials Park, OH, 1992, p. 181.

[19] S. Katsura et al., Corrosion 98 Conference, NACE, paper 132.

[20] S.M. Bruemmer, private communication.

[21] J.T. Busby, G.S. Was, E.A. Kenik, Mater. Res. Soc. Symp. Proc., vol. 540, 1998, MRS Fall Meeting, p. 451.

[22] P.R. Okamoto, L.E. Rehn, J. Nucl. Mater. 83 (1979) 2.

[23] H. Ullmain (Ed.), Atomic Defects in Metals, Landolt-Bornstein, New Series, Group 3, vol. 25, Springer, Berlin, 1991.

[24] E. Simonen, D.J. Edwards, S.M Bruemmer, in: Proceedings of Fall 2000 MRS Meeting, Boston, MA, 2000, p. 2.5.1.

[25] D.R. Olander, Fundamental Aspects of Nuclear Reactor Fuel Elements, Technical Information Center, Energy Research and Development Administration, 1976.

[26] J. Cookson, PhD thesis, University of Michigan, 1996.

[27] A.J. Jacobs, in: A.S. Kumar, D.S. Gelles, R.K. Nanstad, E.A. Little (Eds.), 16th International Symposium On Radiation on Materials, ASTM-STP 1175, ASTM, Philadelphia, 1993, p. 902.

[28] H.M. Chung, W.E. Ruther, J.E. Sanecki, T.F. Kassner, in: D. Cubicciotti (Ed.), Proceedings of Fifth International Symposium On Environmental Degradation Of Materials in Nuclear Power Systems-Water Reactors, ANS, Monterey, CA, 1992, p. 795.

[29] K. Fukuya, K. Nakata, A. Horie, in: D. Cubicciotti (Ed.), Proceedings of Fifth International Symposium On Environmental Degradation Of Materials in Nuclear Power Systems-Water Reactors, ANS, Monterey, CA, 1992, p. 814.

[30] T. Tsukada, Y. Miwa, J. Nakajima, in: R.E. Gold, E.P. Simonen (Eds.), Proceedings of Seventh International Symposium On Environmental Degradation Of Materials in Nuclear Power Systems – Water Reactors, Breckenridge, CO, 1999, 1995, p. 1009.

[31] A. Jacobs, C.M. Sheperd, G.E.C. Bell, C.P. Wozaldo, in: D. Cubicciotti (Ed.), Proceedings of Fifth International Symposium On Environmental Degradation Of Materials in Nuclear Power Systems-Water Reactors, ANS, Monterey, CA, 1992, p. 917.

[32] H.M. Chung, W.E. Ruther, J.E. Sanecki, A. Hins, N.J. Zaluzec, T.F. Kassner, J. Nucl. Mater. 239 (1996) 61.

[33] A.J. Jacobs, R.E. Clausing, M.K. Miller, C.M. Sheperd, in: Proceedings of Fourth International Symposium On Environmental Degradation Of Materials in Nuclear Power Systems-Water Reactors, NACE, 1990, p. 14.

[34] P.L. Andresen, F.P. Ford, S.M. Murphy, J.M. Perks, in: Proceedings of fourth International Symposium On Environmental Degradation of Materials in Nuclear Power Systems-Water Reactors, Jekyll Island, GA, August 1989, p. 1 (NACE, Houston, 1990).

[35] E.A. Kenik, J.T. Busby, M.K. Miller, A.M. Thuvander, G.S. Was, in: Material Research Society Symposium Proceedings, MRS Fall Meeting, vol. 540, 1998, p. 445.

[36] D.J. Barber, Ultramicroscopy 52 (1993) 101.

[37] S.J. Zinkle, P.J. Maziasz, R.E. Stoller, J. Nucl. Mater. 206 (1993) 266.

[38] C. Bailat, A. Almazouzi, M. Baluc, R. Schaublin, F. Groschel, M. Victoria, J. Nucl. Mater. 283–287 (2000) 446.